I. Supporting Text

1. Experimental

1.1. Preparation of Li_2S_6 catholyte and Li_2S_2 powders

The Li_2S_6 catholyte was prepared by adding Li_2S and S powders with a molar ratio of 1:5 into diethylene glycol dimethyl ether (DME) and 1,3-dioxolane (DOL) (v:v=1:1), followed by vigorous magnetic stirring. The concentration of the Li_2S_6 catholyte was 0.1 M [S]. The catholyte also contained 1.0 M lithium bis(trifluoro-methanesulfony)imide (LiTFSI) as the lithium salt.

The nominal Li_2S_2 dispersion with 0.5 M [S] was prepared by adding Li_2S and S powders in DME with a molar ratio of 1:1. After resting for 5 h, the liquid solution was removed by a pipette, followed by drying the powders naturally in an Ar filled glovebox.

1.2. Li–S cell assembly

A 2025 coin-type cell was fabricated by using a piece of lithium foil as the anode, a carbon paper with a diameter of 13.0 mm as the cathode substrate, the Li_2S_6 catholyte as active species, and a PP membrane as the separator. 30 μL Li_2S_6 catholyte was added in the cathode side and 10 μL blank electrolyte (1.0 M LiTFSI in DOL/DME with volume ratio of 1:1) was added in anode side to wet the lithium anode.

As a proof-of-concept trial of enhancing discharge capacity of Li–S cells, Li_2S_8 catholyte with a concentration of 4.0 [S] mol L^{-1} and free-standing carbon nanotube (CNT) scaffold with a specific surface area of 242 m^2 g^{-1} were used as the sulfur source and cathode substrate, respectively. The Li_2S_8 catholyte was prepared as the similar method of Li_2S_6 catholyte, but with Li_2S and S molar ratio of 1:7. The free-standing CNT scaffold was prepared according to our previous work.[1] The CNT film was cut into disk with a diameter of 13.0 mm and an areal mass of 0.20 mg cm^{-2}. To fabricate cell, 30.0 μL Li_2S_8 catholyte was added in the cathode side and 10.0 blank electrolyte was added in the anode site to wet the surface of the lithium metal anode.

1.3. Materials characterization

The morphologies of the $Li_2S_{1/2}$ deposits on carbon paper were characterized by a scanning electron microscope (SEM) operated at 3.0 kV with JSM 7401F (JEOL Ltd., Tokyo, Japan). The crystal structure of the products was measured by X-ray powder

diffractometer (D8-Advance, Bruker, Germany) at 40.0 kV and 120 mA with Cu-K$_\alpha$ radiation, with a scan rate of 5$^\text{o}$ min^{-1}. The nitrogen (N$_2$) adsorption/desorption isotherm was recorded using an Autosorb-IQ2-MP-C system (Quantachrome, USA) operated at $-196\,^\circ\text{C}$ (77 K). The specific surface area was determined according to the Brunauer–Emmett–Teller method. Conductivity measurements were performed on disks with a diameter of 13.0 cm using the KDY-1 four probe technique.

II. Supporting Figures
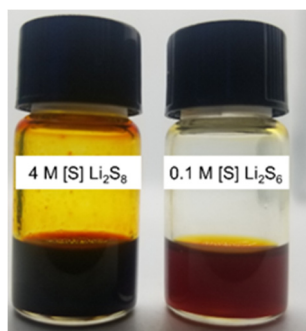
Figure S1. Photograph of Li_2S_6 and Li_2S_8 catholytes with sulfur concentration of 4.0 M and 0.1 M, respectively.
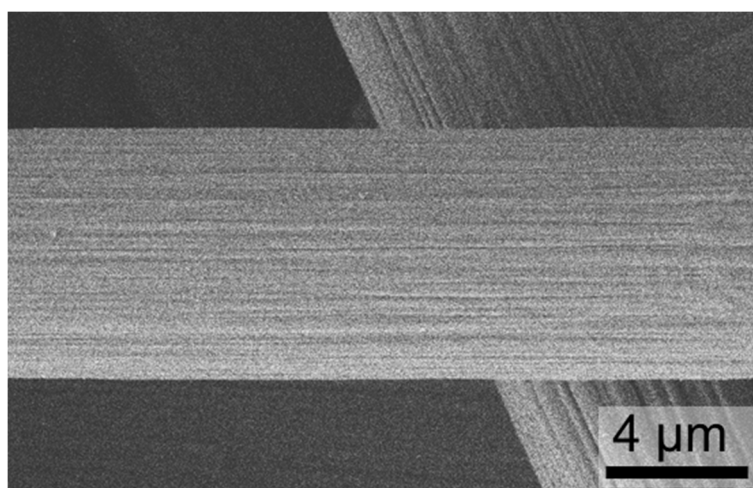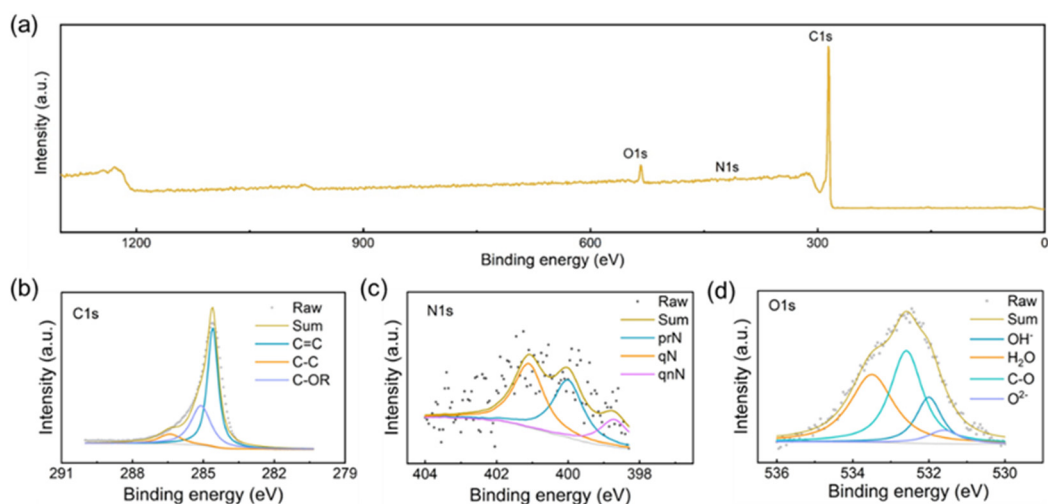
Figure S2. SEM image of carbon paper.

Figure S3. a) XPS survey of CP. High-resolution of b) C1s, c) N1s and d) O1s of CP.

The electrical conductivity of carbon paper measured by a four-probe method was 35.7 S cm^{-1}. The XPS survey showed four peaks at 164, 286, 401, and 535 eV are attributed to S2p, C1s, N1s, and O1s, respectively. The resolved O1s spectrum with O^{2-} (531.6 eV), OH^- (532.0 eV), C-O (532.6 eV) and H_2O (533.5 eV) groups indicates the oxidation of CP in the fabrication process.[2] The presence of a carbonyl group (CO at 285.1 eV) confirms the complexity of oxygen species on the surface of CP. Non-oxygenated carbon bonds (C-C at 286.5 eV and C=C at 284.6 eV) contribute the important electron conductive path for sulfur conversion.[2] The N1s fine scan of CP suggests the nitrogen species of prN (400.1 eV) and pnN (398.7 eV) quaternary N (qN, 401.1 eV). The occurrence of these elemental peaks are due to the functionalization of CP.[3]
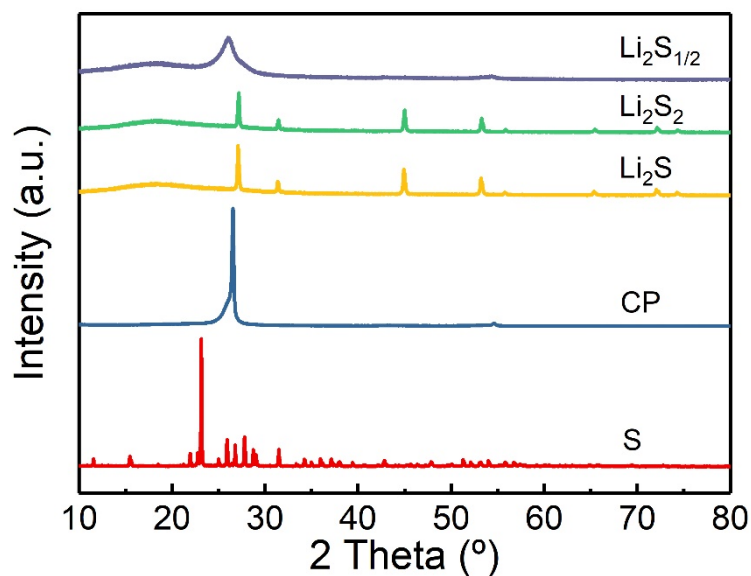
Figure S4. XRD patterns of precipitated $Li_2S_{1/2}$, nominal Li_2S_2, commercial Li_2S powder, CP, and commercial sulfur powder.

$Li_2S_{1/2}$ does not show typical signals due to the amorphous structure and only presents a broad peak at ~26° in the XRD pattern. This peak is most likely suggested to be indexed to the routine CP substrate but with slight changes. Comparing with the routine CP substrate, the peak of precipitated $Li_2S_{1/2}$ on the CP substrate is shifted to a lower angle and become broader probably attributed to the lithiation of CP. The nominal Li_2S_2 was prepared as a reference to confirm the spectrum of $Li_2S_{1/2}$.
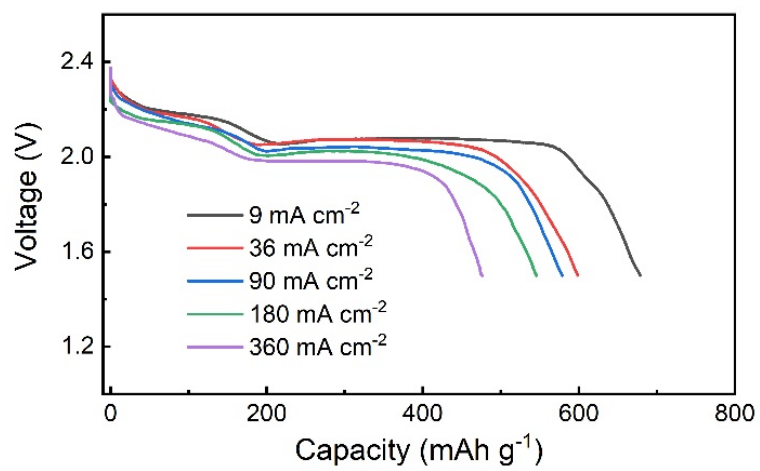
Figure S5. Discharge curves of cells with Li_2S_6 catholyte at different current densities.

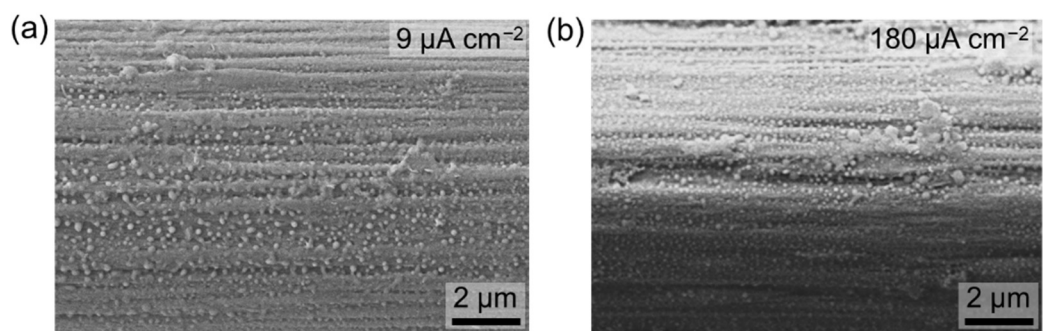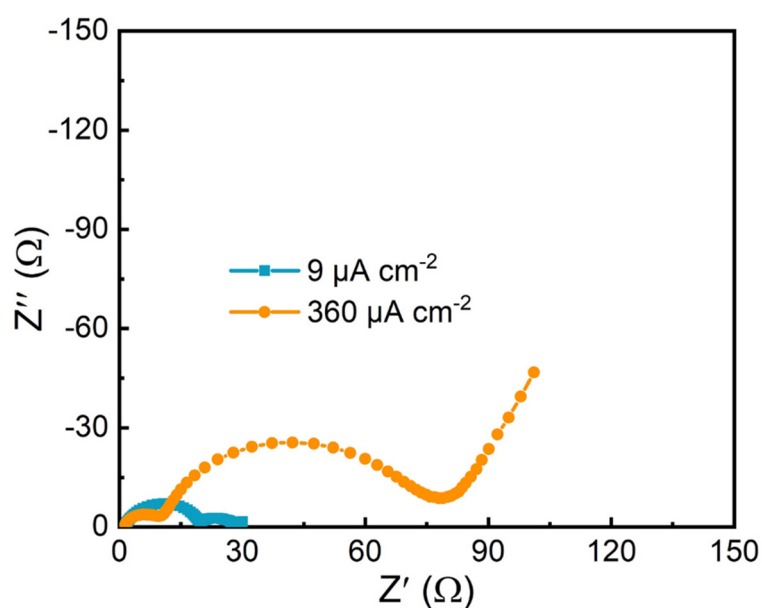**Figure S6.** SEM images of precipitated $Li_2S_{1/2}$ after 10 cycles at a) 9 µA cm^{-2} and b) 180 µA cm^{-2}.

Figure S7. Electrochemical impedance spectroscopy of $Li_2S_{1/2}$ deposits obtained at current densities of 9 and 360 $\mu A\ cm^{-2}$, respectively.

Both cells displayed two-semicircle features. The first semicircle is assigned to the charge transport in the buck $Li_2S_{1/2}$ and the second semicircle represents the interfacial charge transfer among triple-phase boundaries, namely $Li_2S_{1/2}$/substrate/electrolyte. The large particle formed at the small current density affords the long electron transportation in the buck $Li_2S_{1/2}$ and supplies enough triple-phase boundaries, manifesting a higher buck charge transport resistance but a lower interfacial charge transfer resistance than the small $Li_2S_{1/2}$ particles. On the other hand, passivating conductive substrate by the small $Li_2S_{1/2}$ particles inevitably reduces triple-phase boundaries and thus raises the interfacial charge transfer resistance, which is evidenced by the larger second semicircle.
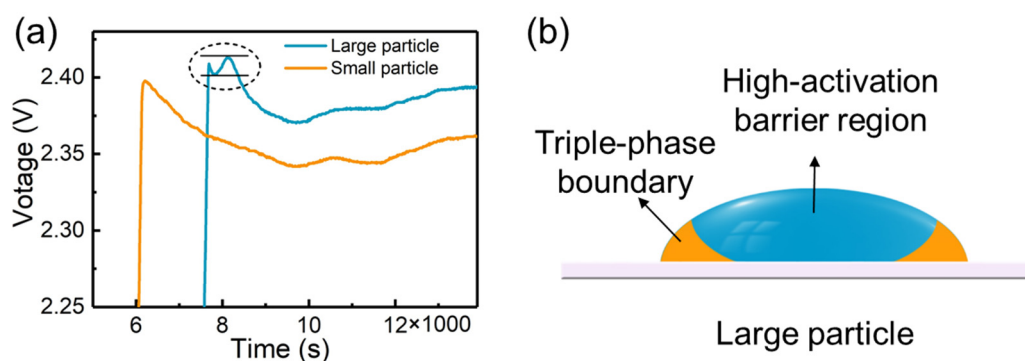
Figure S8. a) Charge curves of $Li_2S_{1/2}$ deposits formed at current densities of 9 (large particle) and 180 (small particle) $\mu A\ cm^{-2}$, respectively. b) Schematic illustration of the voltage hump in the large particle presented in (a).

The charge process of Li–S batteries does not proceed in a complete reverse pathway of the discharge process, since the soluble LiPSs work as a self-redox mediator to promote the oxidation kinetics of $Li_2S_{1/2}$.[4, 5] To decouple the function of LiPSs and reveal the intrinsic effect of particle size on the charge process, the cells discharged at different current densities were disassembled and the carbon paper electrodes with deposited $Li_2S_{1/2}$ were washed by diethylene glycol dimethyl ether (DME) solvent to remove the residual soluble LiPSs. The carbon paper electrode was then re-assembled in a coin cell with a fresh lithium metal anode and electrolyte to evaluate the effect of the deposited $Li_2S_{1/2}$ size on the charge characteristics. The charge current density of both cells were fixed at 36 $\mu A\ cm^{-2}$.

The small-size $Li_2S_{1/2}$ particles obtained at a high current density (180 $\mu A\ cm^{-2}$) display a smooth oxidation of $Li_2S_{1/2}$ without detectable activation barrier. However, the large-size $Li_2S_{1/2}$ particles resulting from the low current density (9 $\mu A\ cm^{-2}$) discharge exhibit a voltage hump (~11 mV) in the charge process (Figure S8a), representing the sluggish oxidation kinetics. The straightforward understanding for the voltage hump is that the charge behavior of $Li_2S_{1/2}$ particles is dominantly determined by the activation area at the triple-phase boundary (Figure S8b).[6] The triple-phase boundary refers to the interface of the $Li_2S_{1/2}$ particles, the conductive scaffolds, and

the organic electrolyte. Considering the insulating nature of $Li_2S_{1/2}$, electrochemical oxidation of the $Li_2S_{1/2}$ particles into LiPSs is restricted at the triple-phase boundary where electron conduction and Li^+ transportation can be simultaneously achieved. The small precipitated particles render a large contact area with carbon substrates, which reduces the electron/Li^+ transport pathways and renders a rapid $Li_2S_{1/2}$–LiPS conversion. Consequently, no voltage hump is observed with a low conversion barrier in this case. On the contrary, the large particles have relatively limited $Li_2S_{1/2}$/substrate/electrolyte triple-phase boundaries that conversion reactions preferably take place, thereby generating increased reaction barriers demonstrated as the voltage hump for residual portion of $Li_2S_{1/2}$ that is far from interfaces. These reaction barriers are responsible for the voltage hump in the charge profile of large precipitated $Li_2S_{1/2}$.
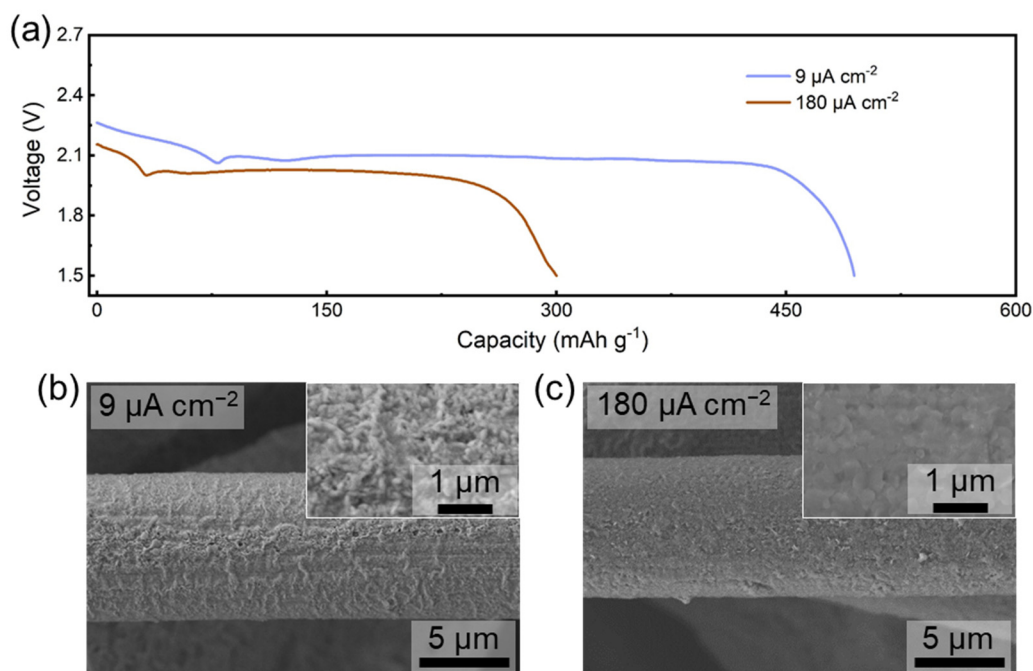
Figure S9. a) Current-density-dependent discharge curves of THF based cells. SEM images of $Li_2S_{1/2}$ deposites at a current density of b) 9 μA cm^{-2} and c) 180 μA cm^{-2}, respectively.

To enrich this study, tetrahydrofuran (THF) solvent was used to verify universality of current-density-dependent $Li_2S_{1/2}$ precipitation. Both high and low current densities render full coverage of thin film $Li_2S_{1/2}$ deposits on CP. Close inspection of $Li_2S_{1/2}$ deposits in a low current density showed that the thin film was composed of nanoparticles. This geometry of $Li_2S_{1/2}$ deposits is quite different from the one that was composed of nano-flake formed at the high current density.
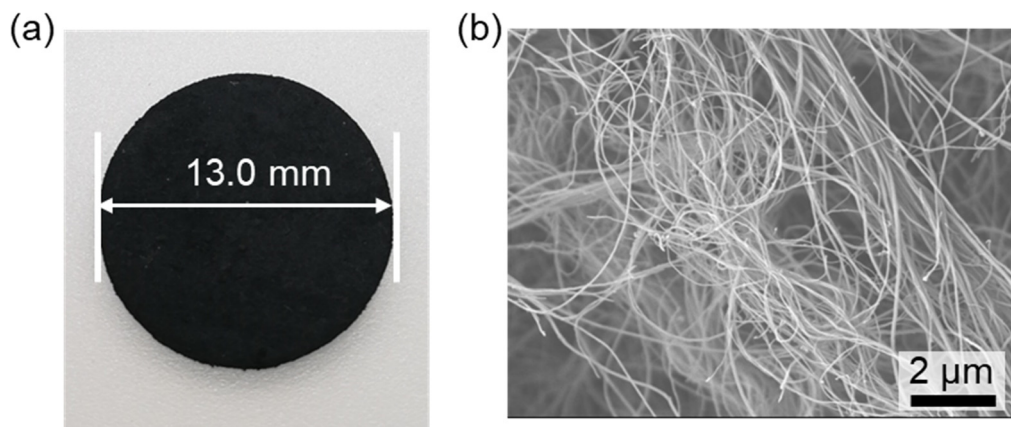
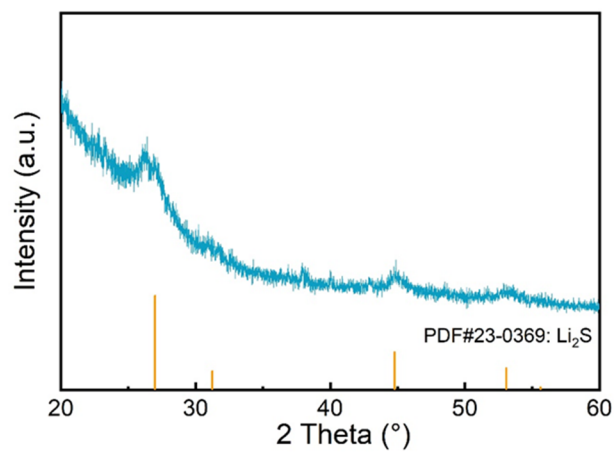**Figure S10.** a) Optical photo and b) SEM image of free-standing CNT scaffold.

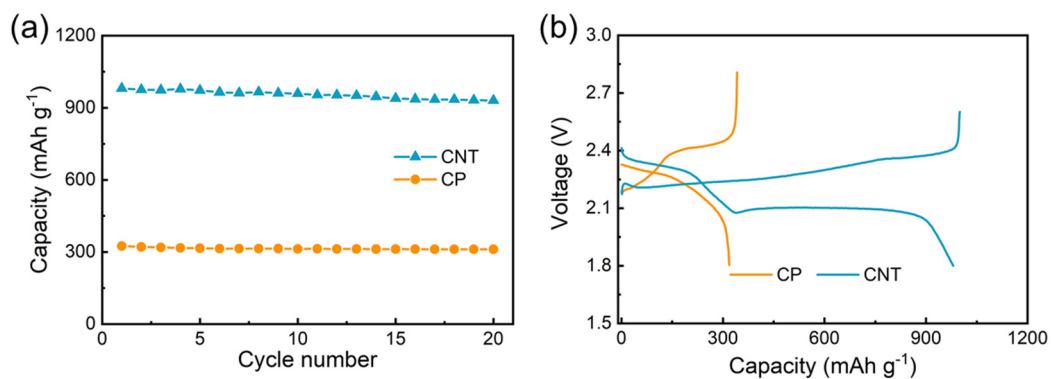**Figure S11**. XRD patterns of discharge products.

Figure S12. a) Cycle performances of Li–S cells with CNT and CP cathode substrates. The sulfur loading in the electrode was fixed at around 1.0 mg cm^{-2} and the current density is 0.5 C based on the sulfur mass. b) Charge and discharge curves of corresponding Li–S cells at the initial cycle.

To verify the importance of specific surface area in the working Li–S batteries, CP and CNT, with specific surface areas of 3.7 and 242 m^2 g^{-1}, respectively, were used as cathode substrates to evaluate battery performances. The same amount of active sulfur was loaded in the cathode substrates and the cells were cycled at a current density of 0.5 C. The cell with the CNT substrate delivered a capacity above 930 mAh g^{-1} after 20 cycles, much higher than the cell with CP substrate (930 mAh g^{-1}). The large capacity gap between these two cells are basically due to the $Li_2S_{1/2}$ precipitation on substrates, since the CP substrate with low specific surface area cannot afford sufficient conductive surface for $Li_2S_{1/2}$ precipitation and thus quickly died before forming insulating $Li_2S_{1/2}$ products.
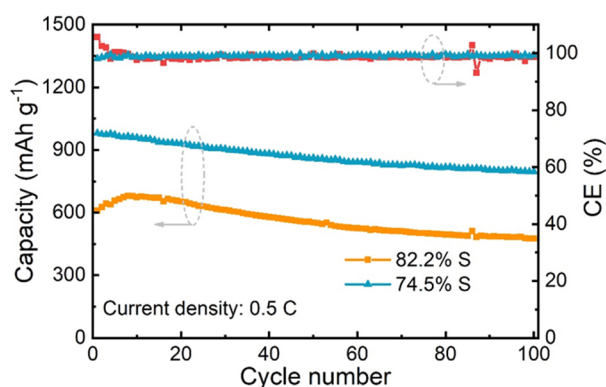
Figure S13. Cyclability of Li–S cells with different sulfur contents.

To balance the sulfur content and battery performances, sulfur contents in the electrode were decreased to 82.2% and 74.5% and these cells were cycled at a relatively high current density of 0.5 C. The cell with 74.5% sulfur content delivered an initial discharge capacity of 981 mAh g^{-1} and preserved a capacity of 797 mAh g^{-1} after 100 cycles, much higher than that of the cell with 82.2% sulfur content (610 mAh g^{-1} at the first cycle *vs.* 476 at the 100th cycle.). The reduction of the sulfur content leaded to much improved sulfur utilization at 0.5 C primarily due to enhanced mobility of sulfur species.
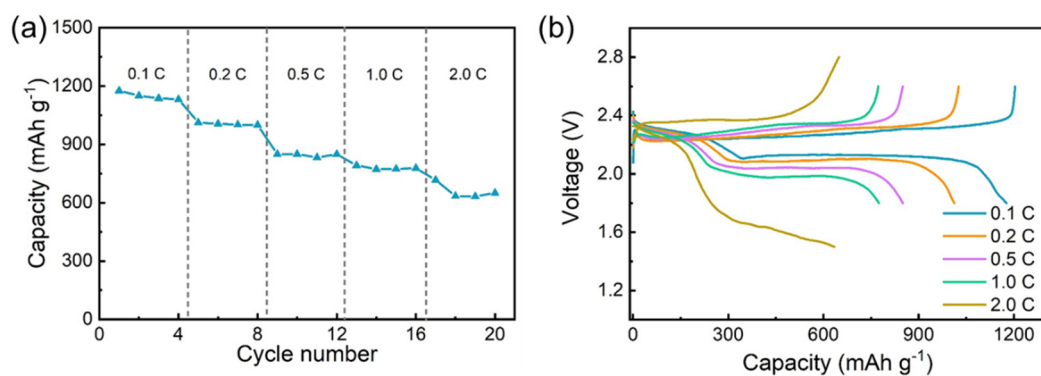
Figure S14. a) Rate capability and b) charge/discharge curves of Li–S cells with a 74.5% sulfur content.

The cell with 74.5% sulfur content can maintain capacities of 773 and 634 mAh g^{-1} even at high current densities of 1.0 and 2.0 C, respectively, (Figure S14a). The presence of the second plateau in the discharge curves at high current densities of 1.0 and 2.0 C (Figure S14b) means the substantial electrochemical conversion from LiPSs to Li_2S_2/Li_2S.
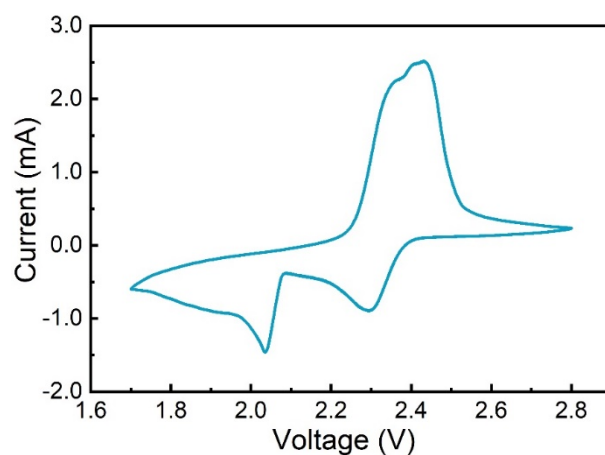
Figure S15. Cyclic voltammetry of the Li–S cell with 74.5% sulfur content.

The step-wise reduction of sulfur to $Li_2S_{1/2}$ through dissolution/precipitation mechanism was confirmed by the cyclic voltammetry measurement, which displayed a clear double-peak feature in the cathodic process.

III. References

1. Z. Yuan, H.-J. Peng, J.-Q. Huang, X.-Y. Liu, D.-W. Wang, X.-B. Cheng and Q. Zhang, *Adv. Funct. Mater.*, 2014, **24**, 6105-6112.
2. Y. Luo, J. Jiang, W. Zhou, H. Yang, J. Luo, X. Qi, H. Zhang, D. Y. W. Yu, C. M. Li and T. Yu, *J. Mater. Chem.*, 2012, **22**, 8634-8640.
3. L. Kong, B.-Q. Li, H.-J. Peng, R. Zhang, J. Xie, J.-Q. Huang and Q. Zhang, *Adv. Energy Mater.*, 2018, **8**, 1800849.
4. Z.-W. Zhang, H.-J. Peng, M. Zhao and J.-Q. Huang, *Adv. Funct. Mater.*, 2018, **28**, 1707536.
5. Q. Wang, J. Zheng, E. Walter, H. Pan, D. Lv, P. Zuo, H. Chen, Z. D. Deng, B. Y. Liaw, X. Yu, X. Yang, J.-G. Zhang, J. Liu and J. Xiao, *J. Electrochem. Soc.*, 2015, **162**, A474-A478.
6. G. Zhou, H. Tian, Y. Jin, X. Tao, B. Liu, R. Zhang, Z. W. Seh, D. Zhuo, Y. Liu, J. Sun, J. Zhao, C. Zu, D. S. Wu, Q. Zhang and Y. Cui, *Proc. Natl. Acad. Sci. USA*, 2017, **114**, 840-845.